Atmos. Meas. Tech. Discuss., 8, 13423–13469, 2015
www.atmos-meas-tech-discuss.net/8/13423/2015/
doi:10.5194/amtd-8-13423-2015

Atmospheric Measurement Techniques Discussions

Thermodynamic correction of particle concentrations measured by underwing probes on fast flying aircraft

R. Weigel[1], P. Spichtinger[1], C. Mahnke[1], M. Klingebiel[2], A. Afchine[3], A. Petzold[4], M. Krämer[3], A. Costa[3], S. Molleker[2], T. Jurkat[5], A. Minikin[5,a], and S. Borrmann[1,2]

[1]Institut für Physik der Atmosphäre, Johannes Gutenberg-Universität, Mainz, Germany
[2]Partikelchemie, Max-Planck-Institut für Chemie, Mainz, Germany
[3]Institut für Energie- und Klimaforschung (IEK-7), Forschungszentrum Jülich, Jülich, Germany
[4]Institut für Energie- und Klimaforschung (IEK-8), Forschungszentrum Jülich, Jülich, Germany
[5]Institut für Physik der Atmosphäre, Deutsches Zentrum für Luft- und Raumfahrt (DLR), Oberpfaffenhofen, Germany
[a]now at: Abteilung Flugexperimente (FX), Deutsches Zentrum für Luft- und Raumfahrt (DLR), Oberpfaffenhofen, Germany

Received: 2 December 2015 – Accepted: 14 December 2015 – Published: 18 December 2015

Correspondence to: R. Weigel (weigelr@uni-mainz.de)

Published by Copernicus Publications on behalf of the European Geosciences Union.

Abstract

Particle concentration measurements with underwing probes on aircraft are impacted by air compression upstream of the instrument body as a function of flight velocity. In particular for fast-flying aircraft the necessity arises to account for compression of the air sample volume. Hence, a correction procedure is needed to invert measured particle number concentrations to ambient conditions that is commonly applicable for different instruments to gain comparable results. In the compression region where the detection of particles occurs (i.e. under factual measurement conditions), pressure and temperature of the air sample are increased compared to ambient (undisturbed) conditions in certain distance away from the aircraft. Conventional procedures for scaling the measured number densities to ambient conditions presume that the particle penetration speed through the instruments' detection area equals the aircraft speed (True Air Speed, TAS). However, particle imaging instruments equipped with pitot-tubes measuring the Probe Air Speed (PAS) of each underwing probe reveal PAS values systematically below those of the TAS. We conclude that the deviation between PAS and TAS is mainly caused by the compression of the probed air sample. From measurements during two missions in 2014 with the German Gulfstream G-550 (HALO – High Altitude LOng range) research aircraft we develop a procedure to correct the measured particle concentration to ambient conditions using a thermodynamic approach. With the provided equation the corresponding concentration correction factor ξ is applicable to the high frequency measurements of each underwing probe which is equipped with its own air speed sensor (e.g. a pitot-tube). ξ-values of 1 to 0.85 are calculated for air speeds (i.e. TAS) between 60 and 260 $\mathrm{m\,s^{-1}}$. From HALO data it is found that ξ does not significantly vary between the different deployed instruments. Thus, for the current HALO underwing probe configuration a parameterisation of ξ as a function of TAS is provided for instances if PAS measurements are lacking. The ξ-correction yields higher ambient particle concentration by about 15–25 % compared to conventional procedures – an improvement which can be considered as significant for many research

AMTD
8, 13423–13469, 2015

applications. The calculated ξ-values are specifically related to the considered HALO underwing probe arrangement and may differ for other aircraft or instrument geometries. Moreover, the ξ-correction may not cover all impacts originating from high flight velocities and from interferences between the instruments and, e.g., the aircraft wings and/or fuselage. Consequently, it is important that PAS (as a function of TAS) is individually measured by each probe deployed underneath the wings of a fast-flying aircraft.

1 Introduction

Clouds constitute one of the most important regulators of the Earth's energy balance. The radiation net effect of various cloud types is not ultimately known yet. The albedo effect and the greenhouse effect of clouds are driven by the cloud element's microphysical properties (e.g. the particles' number, size and shape). In a first order estimate the cloud particle size is mostly determined by the cloud particle number concentration, since the available water vapour for condensation is distributed via diffusion over the number of particles present within a cloud. Cloud particle number concentrations are highly variable (e.g. Krämer et al., 2009), typically ranging between a few thousandths and up to hundreds of particles per cubic centimetre, since specific mechanisms of cloud formation are determined by local dynamics (e.g. Spichtinger and Gierens, 2009; Kärcher and Lohmann, 2002).

Airborne in situ investigations related to the microphysical properties of cloud particles, ice crystals, and hydrometeors are essential for answering many scientific questions and therefore measurement methods by means of underwing probes are widely used (cf. Baumgardner et al., 2011; Wendisch and Brenguier, 2013). Airborne in situ measurements of cloud elements are generally influenced by aerodynamic conditions at the instrument's individual mounting position, i.e. due to specific flow fields around the aircraft's fuselage and wings (Drummond and MacPherson, 1985; Norment and Quealy, 1988). Local fluctuations of the air density may occur in the vicinity of measurement instruments and their sensing volumes (MacPherson and Baumgardner, 1988)

AMTD
8, 13423–13469, 2015

which can affect typical measurements like particle number concentrations and subsequently derived distributions of surface, areas or volumes. Consequently, if possible, the thermodynamic conditions during particle detection need to be considered for gaining accurate and comparable results.

Two scientific missions were carried out in 2014 with the German Gulfstream G-550 (HALO – High Altitude LOng range), the sister ship of the US research aircraft HIAPER (High-Performance Instrumented Airborne Platform for Environmental Research), (Laursen et al., 2006): (1) ML-CIRRUS, from 24 March to 30 April, with a total of ∼ 71 measurement flight hours at mid-latitudes over Central Europe (Voigt et al., 2015), and (2) ACRIDICON-CHUVA, during September, with overall ∼ 96 local mission flight hours in tropical regions, over the Amazonian basin, Brazil (Wendisch et al., 2015). During both missions, several independent underwing probes were deployed (e.g. a Cloud Combination Probe – CCP; a Small Ice Detector – SID3; a Cloud, Aerosol and Precipitation Spectrometer – CAPS; a Cloud and Aerosol Spectrometer – CAS, a Precipitation Imaging Probe – PIP; and the Particle Habit Imaging and Polar Scattering – PHIPS-probe) for studies concerning cloud particle microphysical properties at relative high flight velocities reached by HALO (up to Mach 0.75). Thus, the impact on the air flow conditions towards underwing probes, previously considered numerically for flight velocities between 50 and 130 $\mathrm{m\,s^{-1}}$ (Norment and Quealy, 1988) and empirically for up to 100 $\mathrm{m\,s^{-1}}$ (MacPherson and Baumgardner, 1988), needs to be re-assessed for the air compression accompanied with high flight velocities.

The diagram in Fig. 1 shows an aircraft fuselage under flight conditions when passing a field of enhanced particle concentration, e.g., a cloud. By means of avionic (meteorological) sensors in the air data boom (cf. Fig. 1b; also referred to as nose boom) the ambient static air pressure (p_1) and temperature (T_1) are almost undisturbedly measured. The dynamic pressure proportion provided by the aircraft avionic sensors is transferable into the True Air Speed (TAS) according to Bernoulli's law and describes the aircraft velocity relative to the current motion of air.

AMTD
8, 13423–13469, 2015

The underwing instrument probes are contained inside Particle Measuring Systems (PMS) standard canisters (with outer diameter of ~ 177 mm) which, in the HALO configuration, are pairwise mounted at an underwing pylon such that the instrument is placed 360 mm (±30 mm) underneath the aircraft wings. The instruments' detection volume is positioned ~ 100 mm upstream of the wing's leading edge. The instruments' probe head has a quasi-aerodynamic shape (individual probe head designs of three different instruments are shown in Fig. 5). The individual probe head of the respective instrument is additionally characterised by extension arms that include the detection laser optics or other annexes such as, e.g., the CAS winglet. Although the probe heads are generally of streamlined shape the moving probe constitutes a flow resistance during flight due to the instrument body's cross-sectional-area perpendicular to the direction of the air flow (cf. Fig. 1a). Thus, a compression region forms in a distance of 0.3–0.5 m upstream of the probe head (Wendisch and Brenguier, 2013) and the strength of compression is a function of aircraft speed. Further flow-dynamical influences resulting from the proximity of the instruments to the wings or the fuselage of an aircraft may contribute to the modifications on the flow conditions (Drummond and MacPherson, 1985; MacPherson and Baumgardner, 1988). Primarily, the air compression due to the moving instrument body decelerates the air speed measurable at the probe, as the Probe Air Speed (PAS), whereby the rate of deceleration is a function of TAS. Furthermore, the compression of air results in the densification of the airborne particles at the point of measurement, i.e. well inside the compression region. This means that the particle concentrations measured under compressed conditions need to be scaled to ambient condition.

We aim at formulating an expression that is based on a thermodynamic approach to provide a correction factor for inverting measured particle number concentrations to ambient conditions. The variables contained in the corrective expression should be available from meteorological data that are generally measured during research flights. Further variables of the measurement conditions should be available from the instrument itself, provided that it is equipped with a pitot-tube. The effective correction may

AMTD
8, 13423–13469, 2015

vary for the different instruments, the aircraft type and the position of the probe relative to the aircraft wings and/or fuselage. However, if the instrument is not equipped with a pitot-tube, or the pitot-tube is inoperative, the air speed at the point of measurement is unknown. In such a case the herein provided parameterisation of the compression correction serves as a guideline for adopting the TAS from the aircraft data after adjustments. In the following the application of both, the derived thermodynamic correction and the unadjusted aircraft TAS on a data set of atmospheric measurements, illustrates the sensitivity of the results to the employed procedure. Furthermore, we show that the thermodynamic correction is relatively insensitive to the instrument position with respect to the aircraft fuselage, and the correlations of instrument-specific correction factors demonstrate robustness and consistency of the suggested approach.

2 Method

In this section, we describe a new method for determining the number concentration of particles in a given air volume from measured quantities and from basic thermodynamics. We will particularly emphasise the difference between our approach and the conventionally used methods which focus exclusively on geometrical considerations, but neglects effects of air compression.

For the following examination some definitions need to be particularly introduced: All velocities that are specified as air speeds (v_1, v_2, TAS, PAS) and the velocities of particles (v_p) refer to the moving aircraft or instruments relative to the air as the reference system. Measurement conditions are those under which the measurement occurs in the detection region that is impacted by compression. Ambient (undisturbed) conditions relate to the initial state far away from the aircraft.

AMTD
8, 13423–13469, 2015

2.1 Ambient vs. measured particle number densities

The measured number concentration N_{meas} (in units of number per air volume) detected with underwing probes that have a free stream detection volume is defined as:

$$N_{meas} = n \cdot \frac{1}{A_s \cdot v_p} \cdot \frac{1}{\Delta t} = \frac{n}{V_{meas}}. \quad (1)$$

Here, n denotes the number of particles detected during the time interval Δt (in s), and v_p denotes the velocity (in $m\,s^{-1}$) of particles penetrating the sample area A_s (in m^2).

In good approximation it can be assumed that $v_p \approx PAS = v_2$. The detection volume is therefore defined as:

$$V_{meas} = A_s \cdot v_2 \cdot \Delta t. \quad (2)$$

The ambient particle number concentration in the undisturbed ambient air is given as:

$$N_{amb} = \frac{n_{amb}}{V_1} \quad (3)$$

with the number of particles n_{amb} and the ambient air volume V_1 (in m^3).

Due to the compression of air upstream of the instruments, the ambient volume V_1 converts into the volume V_2. Under the presumptions that the particle number per mass M of the air sample is not affected by compression (i.e. remains constant and thus: $\frac{n_{amb}}{M} = \frac{n_{meas}}{M}$), that the particles' inertia is negligible for given streamlines, and that the ideal gas law ($p \cdot V = M \cdot \mathbf{R}_s \cdot T$; with $[p] = kg\,m\,s^{-2}$, $[V] = m^3$, $[M] = kg$, $[T] = K$) applies and where $\mathbf{R}_s$ denotes the specific gas constant (in $J\,kg^{-1}\,K^{-1}$; while $J = kg\,m^2\,s^{-2}$) we end up with the following equation:

$$\frac{n}{M} = \text{const.} \Longrightarrow n_{amb} \frac{\mathbf{R}_s \cdot T_1}{p_1 \cdot V_1} = n_{meas} \frac{\mathbf{R}_s \cdot T_2}{p_2 \cdot V_2}. \quad (4)$$

AMTD
8, 13423–13469, 2015

Then we can derive the expression for determining the ambient particle number concentration:

$$N_{amb} \cdot \mathbf{R}_s \cdot \frac{T_1}{p_1} = N_{meas} \cdot \mathbf{R}_s \cdot \frac{T_2}{p_2} \xrightarrow{v_p = v_2} N_{amb} = N_{meas} \cdot \frac{p_1}{p_2} \cdot \frac{T_2}{T_1}. \quad (5)$$

2.2 TAS-based particle number concentrations

If the air speed at the probe (PAS, v_2) during measurements is unknown, e.g. for the case that the probe is not equipped with a pitot-tube or when a present pitot-tube is frozen, it is common practice to presume the particle speed (v_p) to equal the true air speed (TAS, v_1) to determine particle number concentrations (cf. Eq. 1).

Equivalent to using the TAS, the same resulting concentration is achieved when alternatively using the velocity ratio $\frac{PAS}{TAS}$ (i.e. $\frac{v_2}{v_1}$) as the factor for multiplication with measured particle number concentration (N_{meas}, cf. Eq. 1), i.e.:

$$N_{meas} \cdot \frac{v_2}{v_1} = \frac{n}{A_s \cdot t \cdot v_2} \cdot \frac{v_2}{v_1} = \frac{n}{A_s \cdot t \cdot v_1}. \quad (6)$$

If pitot-tube measurements of PAS are available, the treatment of resulting N_{meas} with the factor $\frac{PAS}{TAS}$ lacks any physical rationale and relies only on the geometrical consideration that $V_1 \cdot t^{-1} = TAS \cdot A_s$ and that $V_2 \cdot t^{-1} = PAS \cdot A_s$. Nevertheless, as both procedures yield identical results with the same error level, in the following the use of TAS for determining a particle number concentration is treated synonymously to correcting N_{meas} (as defined in Eq. 1) by the factor $\frac{PAS}{TAS}$.

This approach results in significantly underestimated particle number concentrations with respect to the ambient conditions for following reasons.

1. By presuming v_1 as the speed of particles while penetrating A_s it is insinuated that a certain number of particles per Δt was detected while probing a linearly enlarged air volume per Δt. Resulting enlargement would describe an expansion

AMTD
8, 13423–13469, 2015

that is in-line with the flight direction. However, thereby the volumetric compression occurring in reality is not accounted for.

2. The ratio of air speeds $\frac{\mathrm{PAS}}{\mathrm{TAS}}$ solely results from the dynamic pressure proportions, or rather the ratio thereof, obtained from respective air speed sensor, the data boom and the instrument's pitot probe. The compression upstream of the instrument, however, should predominantly impact the absolute pressure at the point of measurement in comparison to ambient conditions, although the compression is dynamically induced.

Indeed, it needs to be taken into account that the compression of air upstream of the probe induces changes in a particles' motion out of the initially undisturbed ambient state. Thus, at the point of detection the changed particle motion excludes the use of v_1 to describe the particle velocity through the detection region of the instrument.

Instead, the particles can be assumed to pass the instruments detector with a velocity that is better described by v_2 which is generally smaller (by up to 30 %) than v_1. Strong indications for the trustworthiness of recorded v_2 (PAS) are given by the imaging technique of CIP-type instruments (also referred to as OAPs – Optical Array Probes). This instrument type records image slices by means of a linear diode detector for subsequent reassembling to full 2-D images of respective particles. The scanning frequency and imaging rate of the linear diode detector is triggered by the air speed measured by the probe's pitot-tube. Consequently, a significant deviation or falsification of this PAS measurement would result in distorted images. Laboratory calibrations are regularly performed by using a spinning disc of known rotation speed. Non-transparent circular spots on the disk are moved through the instruments sample area to simulate penetrating particles. The calibrations at relatively low penetration speeds ($\sim$ 23–25 $\mathrm{m\,s^{-1}}$) compared to airborne measurements reveal that a deviation of the probe-measured air speed considerably exceeding 10 % relative to the disc speed already causes a visible deformation of taken images as illustrated in Fig. 2. The strength of image distortion as a function of air speed deviation can be expresses by the aspect

AMTD
8, 13423–13469, 2015

ratio of the taken images (Fig. 3) from a circular object that penetrates the instrument's detection region when the probe is calibrated with the spinning disc. The relationship between the image aspect ratio and the percentage of PAS deviation is almost linear which appears to be plausible as the diode array scanning frequency should be proportional to the values of PAS. Thus the deviation between PAS and particle penetration speed exhibits a linear relationship with the image aspect ratio. Appropriate analyses of images taken from initially spheroidal particles, i.e. from droplets, may suffice for qualitatively evaluating measured PAS compared to the factual particle penetration speed. At higher air speeds (e.g. up to 250 m s^{-1} for HALO) it is expected that even smaller uncertainties of measured PAS related to the true particle penetration speed cause severe distortion of resulting images. Thus, for measured v_2 we assume the uncertainty to range within ~ 10 % if recorded particle images of droplets or spheroids do not systematically exhibit a strong and, therefore, obvious deformation.

The ability of particles to get adapted to changes in air speed depends on the particle size, mass and inertia and can be expressed by the calculable relaxation time (Hinds, 1999; Kulkarni et al., 2011; Willeke and Baron, 1993, respectively). Cloud particles, for example, of sizes smaller than 100 µm diameter, moving with 70 m s^{-1} at atmospheric pressures of 300 hPa and temperatures of 240 K, have relaxation times (at the most 9 ms) in the same order of magnitude as the compression time scales (2–4 ms at flight speeds from 125 to 250 m s^{-1}, cf. Paragraph 3.2). For judging the ability of larger cloud particles to adapt to changes in air speed more than 200 particle images from one flight "AC13" during the HALO mission ACRIDICON-CHUVA (for further details see paragraph 3.4) were analysed. Note that the maximum flight speed during this flight was ~ 220 m s^{-1} and that about one quarter of the flight was performed at flight speed between 120 and 140 m s^{-1}. The aspect ratio of images taken from presumably spheroid cloud particles were charted as a function of particle size. The images of spheroidal objects were selected due to their particular symmetry and shading intensity that stand out from the image properties of other cloud elements such as for example irregular or plane ice particles. Random samples were taken well distributed over the

AMTD
8, 13423–13469, 2015

data recorded during the complete flight, regardless of the flight altitude or flight speed. Generally, particles with diameter greater than 50 µm were analysed, mostly 2–5 images in consecutive order before selecting a new measurement period. Occasionally also droplet images were measured (~ 20 % of all analysed images) that were singularly present in a particle population that was either dominated by much smaller cloud elements (~ 20–40 µm) or by much larger precipitation particles (usually loose, amorphous ice agglomerates of diameter > 600 µm). Figure 4 depicts the result of these analyses. The scatter of the single data points (Fig. 4a) is statistically processed by means of the aspect ratio median with percentiles (10, 25, 75 and 90 %) in particle diameter size bins of 30 µm (Fig. 4b). Images of particles with diameter smaller than 100 µm show distortions within 10 % which is synonymous for a v_2-PAS-deviation of less than 10 % (cf. Fig. 3). For droplets of diameter between 100 and 250 µm the image aspect ratios increasingly scatter, but the resulting median does not indicate that v_2 deviates from PAS by more than 10 %. Moreover, for the same droplet size range, a v_2-PAS-deviation of less than 15 % is suggested by 75 % of the data points. The images of particles with diameter larger than 250 µm exhibit increasing distortion as the image aspect ratios approach values suggesting a v_2-PAS-deviation of up to 20 %. However, none of the analysed images exhibits an aspect ratio of about 0.75 which should systematically be the case if v_2 was coincident with TAS. The observations provide the hint that the driving forces arising in the flow field upstream of an underwing probe overcome the inertia resistance even of larger cloud elements of diameter > 100 µm. This supports the suggestion that the penetration speed of the vast majority of detected particles through an OAP's detection region may be better described by the PAS (v_2), rather than by the TAS (v_1).

Hence, we conclude that

a. the compression of air causes a densification of airborne particles in the detection region of the considered instrument,

AMTD
8, 13423–13469, 2015

b. the compression is reflected by systematically lower values of v_2 (PAS) compared to v_1 (TAS), exhibiting a discrepancy that is too large to be covered by a 10 % uncertainty of measured PAS,

c. the particles' velocity while passing the instrument sample area is best approximated with v_2, rather than with v_1, and

d. the conventionally applied practice of treating N_{meas} with the factor $\frac{PAS}{TAS}$ (geometric approach) is invalid for correcting measured number concentration to ambient conditions,

e. a method is needed to reasonably correct N_{meas} by accounting for the air compression, particularly at high flight velocities, to determine N_{amb}.

2.3 Correction of N_{meas} based on thermodynamic considerations

The expression that accounts for the described compression effect is formulated in its general form with Eq. (5). The unknown parameter in this expression is the probe air temperature T_2 that is increased in comparison to ambient air temperature T_1 as a consequence of the compression. The temperature increase is obtainable by using Bernoulli's law together with the ideal gas law and, furthermore, by presuming adiabatic conditions, i.e. the conservation of energy. The derivation emanates from following different conditions which are illustrated in Figure 1 for the air velocity v, the air pressure p, the specific enthalpy h of a uniform system and the gravitational potential ϕ:

condition 1 – at the aircraft's air data boom: $v_1, p_1, T_1, h_1, \phi_1$

condition 2 – upstream of the probe: $v_2, p_2, T_2, h_2, \phi_2$

Bernoulli's law for compressible gases and under the presumption of energy conservation reads as:

$$\frac{1}{2}v_1^2 + h_1 = \frac{1}{2}v_2^2 + h_2, \tag{7}$$

AMTD
8, 13423–13469, 2015

assuming that the gravitation potential $\phi_1 = \phi_2$ since the relative elevation between the air data boom and the underwing probe position is negligibly small, i.e. < 10 m.

For finite differences of the specific enthalpy ($\Delta h = h_2 - h_1$) one can use:

$$\Delta h = c_p \Delta T. \tag{8}$$

wherein c_p denotes the specific heat capacity (in $\mathrm{J\,kg^{-1}\,K^{-1}}$).

For the further derivation we assume the following:

a. The pressures p_1 (static air pressure) and p_2 (static air pressure at the probe during measurement) are measured with sufficient certainty.

b. For velocities relative to undisturbed ambient cloud conditions the velocity v_1 equals the avionic TAS while v_2 is the air speed determined from the probe's pitot measurements, PAS.

c. Under undisturbed ambient conditions, for which p_1 and T_1 are valid, the particles' initial velocity relative to the aircraft flight direction may be close to zero, or at least much smaller than v_1 and v_2.

d. Unless distortion of recorded images of spheroidal particles is obvious the presumption is valid that during measurements the particles' velocity is well approximated with v_2 in the compression region where the probe measurement occurs.

Subsequently, Eq. (7) leads to

$$\frac{1}{2}\left(v_1^2 - v_2^2\right) = h_2 - h_1 = c_p \Delta T = c_p (T_2 - T_1). \tag{9}$$

Hence, rather than the velocity ratio (cf. Sect. 2.2), the difference of the squared velocities appears in the thermodynamic approach. With Eq. (9) the functional relationship between the aircraft air speed, reduced by the compression-induced airflow velocity during measurement, i.e. the expression $v_1^2 - v_2^2$, is provided vs. the relative heating of

AMTD
8, 13423–13469, 2015

the probed air with respect to ambient conditions. Consequently, the resulting squared velocity difference implies the change of the particles' motion in-line with the flight direction due to the compression.

Rearrangement of Eq. (9) leads to:

$$T_2 = T_1 + \Delta T = T_1 + \frac{1}{2 \cdot c_p}\left(v_1^2 - v_2^2\right). \tag{10}$$

The specific heat capacity c_p of air ranges from about 1002.5 to 1006.4 $\frac{\mathrm{J}}{\mathrm{kg \cdot K}}$ for atmospheric temperature conditions between 180 to 325 K (Dixon, 2007). Accepting an implied uncertainty in the per-mill-range, the product $2 \cdot c_p$ in Eq. (10) may be replaced by 2008 $\frac{\mathrm{J}}{\mathrm{kg \cdot K}}$.

Implying T_2 from Eq. (14) into Eq. (5) leads to the thermodynamic correction of measured particle number concentrations to account for the compression of air upstream of the probe during flight:

$$N_{\mathrm{amb}} = N_{\mathrm{meas}} \cdot \frac{p_1}{p_2} \cdot \left(1 + \frac{1}{2008 \frac{\mathrm{J}}{\mathrm{kg \cdot K}} \cdot T_1}\left(v_1^2 - v_2^2\right)\right) = N_{\mathrm{meas}} \cdot \xi. \tag{11}$$

By means of Eq. (11) the thermodynamic correction factor ξ is introduced, which basically equals the ratio of the probed volume and according ambient volume ($\frac{V_2}{V_1}$) of air and which is used for the following discussions. Note that the temperature ratio included in ξ still depends on the air speeds v_1 (TAS) and v_2 (PAS). Insinuating an uncertainty of measured PAS of ±20 %, which is unrealistically high as resulting distortions in the particle images were highly visible (cf. Sect. 2.2 and Fig. 2), the resulting error of calculated T_2 is at most ±3 % which influences the absolute effectiveness of ξ negligibly (cf. Sect. 3.2). Hence, with ξ the sensitivity of a correction factor to uncertainties in measured PAS is reduced, whereas the air speed ratio $\frac{\mathrm{PAS}}{\mathrm{TAS}}$ is unabatedly affected by any uncertainty in measured PAS.

AMTD
8, 13423–13469, 2015

3 Applying the compression correction to airborne measurements

It is plausible that the magnitude of compression increases with air speed, i.e. with flight velocity. Thus, the derived thermodynamic correction should have the largest effect on data acquired during flights with fast aircraft, for example with the Learjet-35A, the Gulfstream G-550 HALO or HIAPER (up to Mach 0.75, corresponding to $\sim 250\,\mathrm{m\,s^{-1}}$). The extent of such corrections underlying both, the geometric and the thermodynamic perspective, and their impact on the measured data are discussed in the following for actual measurements from three (out of eight) underwing probes deployed on the HALO aircraft.

3.1 Instrumentation related to cloud particle microphysics

The three selected instruments are PMS-type underwing probes which are commercially available from the instrument manufacturer Droplet Measurement Technologies (DMT, Boulder, CO, USA) with the general purpose of investigating the microphysical properties of cloud elements and hydrometeors. One particular measurement technique the three instruments have in common is based on the principle of Optical Array Probes (OAP) as described by Knollenberg, 1970. Advanced developments of the OAP measurement method led to the shadow cast imaging instruments of different types (Korolev et al., 1991, 1998; Korolev, 2007; Lawson et al., 2006) that are currently in use. The HALO underwing probes to be discussed are:

1. The Cloud Combination Probe (CCP) combines two detectors:
    a. the Cloud Droplet Probe (CDP), detecting forward scattered laser light due to particles penetrating the CDP detection area (Lance et al., 2010) as an advanced development of the Forward Scattering Spectrometer Probe (FSSP) technique (cf. Dye and Baumgardner, 1984, Baumgardner et al., 1985; Korolev et al., 1985), and

AMTD
8, 13423–13469, 2015

b. the Cloud-Imaging Probe greyscale (CIPgs) that records 2-D shadow cast images of cloud elements that cross the individual CIPgs detection region.

CCP measurements overall cover a particle diameter size range from 2 to 960 µm. The performance of the specific CCP instrument used in this study is demonstrated by earlier investigations related to clouds in the tropical convective outflow (Frey et al., 2011), concerning Polar Stratospheric Clouds (PSC) (Molleker et al., 2014) or within low level mixed-phase clouds in the Arctic (Klingebiel et al., 2015) when deployed at much slower flight velocities ($< 170\,m\,s^{-1}$).

2. The Novel Ice eXpEriment – Cloud, Aerosol and Precipitation Spectrometer (NIXE-CAPS) described by Meyer, 2012 also combines two measurement techniques:

   a. The CAS-DPOL module (Cloud and Aerosol Spectrometer) is based on the principle of forward scattering detection similar to the CDP (cf. above), but, instead of using an open path detection region (CDP), the CAPS is equipped with an inlet tube. In addition, the CAS-DPOL discriminates between spherical and aspherical particles by measuring the change of polarisation of laser light that is scattered by single particles (cf. Baumgardner et al., 2001, 2014).

   b. Additionally, NIXE-CAPS is equipped with a CIPgs instrument (cf. CCP).

With NIXE-CAPS cloud particles with diameters between 0.6 and ∼ 950 µm are detected. Note that the thermodynamic correction derived here applies as such to particle number concentrations measured particularly with the OAPs (the CIPgs probes and the PIP) since the flow conditions inside the inlet tube of the CAS-DPOL differs from those of the open path instruments.

3. The Precipitation Imaging Probe (PIP):

The PIP detects precipitating cloud elements and hydrometeors by means of particle-induced shadow projection onto a diode sensor allowing for a 2-D particle imaging

AMTD
8, 13423–13469, 2015

similar to the CIPgs. In comparison to the CIPgs, the PIP setup features an increased detection volume covering larger particle sizes with 100 µm < D_p < 6400 µm.

One major difference between CCP, NIXE-CAPS and PIP is the instrument-specific design of the probe heads. As shown in Fig. 5, CCP is equipped with a 90°-angled wedge. NIXE-CAPS combines a wedge of the same shape with an additional aerodynamic winglet that may significantly contribute to the effective cross-sectional area of the NIXE-CAPS body. PIP is equipped with a half-sphere front cap. The different instrument heads have specific extension tips. Between the tips a free laser beam crosses the freely flowing sample air through which the particles pass. The sample area A_s of the probes, where the instrument is sensitive for particles crossing the open laser beam, is located almost half way between the tips.

One further important difference of the three instruments is their mounting position with respect to the aircraft fuselage (cf. Fig. 1b). PIP is mounted closest to the aircraft fuselage under the portside wing. NIXE-CAPS and CCP are positioned under the starboard wing on the intermediate and outbound hardpoints, respectively. Thus, with the three selected instruments the full range of available underwing probe positions with respect to the aircraft fuselage of HALO is covered.

3.2 Specific correction factor ξ for HALO instruments

The continuous measurements of the parameters v_1 (TAS), v_2 (PAS), T_1 (static air temperature), p_1 (static ambient pressure) and p_2 (static pressure at the probes) during flight allow for deriving the factors for the geometric correction $\frac{\mathrm{PAS}}{\mathrm{TAS}}$ and the thermodynamic correction ξ as a function of TAS with 1 Hz temporal resolution. Hence, individual ξ-corrections are obtainable at any time during the measurement with pitot-equipped instruments. Figure 6 shows the comparison of calculated ξ and $\frac{\mathrm{PAS}}{\mathrm{TAS}}$ corrections (synonymous for using TAS instead of PAS for N_{meas}, cf. Sect. 2.1) as a function of TAS. The unadjusted data from 6 out of a total of 11 ML-CIRRUS flights are shown. In sum, for the following, the 1 Hz-resolved data of more than 35 flight hours are treated.

AMTD
8, 13423–13469, 2015

During the flight on 29 March 2014 (red data points) the factors $\frac{PAS}{TAS}$ and ξ as a function of TAS occasionally show significant deviation from the generally observed course. This deviation can unambiguously be apportioned to disturbed PAS measurements. The PAS chart is subject to disturbances either due to freezing conditions causing the pitot-tube to be tamped or due to non-isoaxial airflow caused by flight manoeuvers like tight turns. Very few and relatively short periods of PAS disturbances also occurred during the flight on 11 April 2014 (pink data points).

The ξ-correction is a monotonous function of flight velocity that has increasing effectiveness for each of the three instruments. Contrarily, the $\frac{PAS}{TAS}$ correction appears to be systematically effective over the full range of air speeds, even at the lowest aircraft velocities – while the scatter of $\frac{PAS}{TAS}$ by ∼ 2–10 % may result from small scale turbulences or non-isoaxial airflow. However the geometric correction with $\frac{PAS}{TAS}$ causes a general reduction of the values measured with CCP and NIXE-CAPS of not less than 20 %, even reaching 35 % for NIXE-CAPS (cf. Fig. 6). For CCP the values of ξ and $\frac{PAS}{TAS}$ are most compact. The variability, in particular of $\frac{PAS}{TAS}$, increases for NIXE-CAPS over the complete TAS-range. For PIP the ξ-factor is comparably variable at flight velocities greater that 140 m s^{-1}. In comparison with the other probes the most severe differences were found for the correction factors of the PIP. Here, the geometric correction with $\frac{PAS}{TAS}$ exhibits the highest effectiveness (∼ 20 %) for lowest flight speeds and decreases with increasing velocities up to 190 m s^{-1} (∼ 10 %). At a certain point (TAS ≈ 190 m s^{-1}) the degree of correction with $\frac{PAS}{TAS}$ takes a sharp turn and climbs again as higher air speeds are reached. For TAS-values greater than 190 m s^{-1} a correction with $\frac{PAS}{TAS}$ would not strongly deviate from a correction made with corresponding ξ-factor.

The events when the pitot-tube was frozen or affected by misaligned inflow (mainly attributed to the measurements made on 29 March 2014 and to a limited number of measurements made on 11 April 2014) were removed from the data set which effectively reduces the data set volume by less than 3 %.

AMTD
8, 13423–13469, 2015

For CCP measurements (data set as treated for Fig. 6) the parameters for calculating ξ according to Eq. (11) are shown in Fig. 7a as a function of TAS. Displayed are the absolute differences of measured pressures (p_1, p_2) and velocities (v_1, v_2). The difference of the squared velocities v_1 and v_2 (Eq. 11) is implicitly included in calculated T_2. Moreover the difference between measured temperature T_1 and the calculated temperature T_2 is shown. At a maximum TAS of 255 m s^{-1} the compression impact causes a Δv of up to 75 m s^{-1}, a ΔT of up to 16 K and a Δp of about 30–60 hPa. In Fig. 7b the results of the pressure expression $\frac{p_1}{p_2}$ (green data points) and temperature fraction $\frac{T_2}{T_1}$ (black data points), as applied in Eq. (11), is displayed as a function of TAS, illustrating the respective effectiveness of each term to calculated ξ.The inversion to N_{amb} causes N_{meas} to be reduced by a factor of up to 0.8 to compensate for the induced pressure increase. In contrast, the compression-induced heating of air needs to be corrected by a factor of up to 1.07.

Remark: For a TAS_{max} of 255 m s^{-1} the compression-induced heating increases the temperature of the air sample by a ΔT_{max} of 16 K. Assuming that the air gets compressed over a distance of ~ 0.5 m upstream of the instrument (cf. Wendisch and Brenguier, 2013, Sect. 6.2.1 therein) then, for the given flight velocity, the airborne particles are exposed for an overall duration of about 2 ms to a continuously heating environment, ending up at the ΔT_{max} of 16 K. The shrinkage of an airborne ice particle of 2 µm initial size diameter is at most ~ 5 % after a 2 ms lasting exposure to a ΔT_{max} of 16 K (at any initial air temperature of 190–245 K) at a static pressure of 300 hPa, as calculated from the mass rate change (Pruppacher and Klett, 2012; Spichtinger and Gierens, 2009). The shrinkage increases vigorously for particle of initial sub-micron size. Moreover, the compression of air over a distance of ~ 0.5 m upstream of the instrument causes a Δp_{max} of 60 hPa (cf. Fig. 7a). If scaled to the dimensions of a droplet of millimetre-sized diameter (smaller particles are affected to lesser extent) the potential droplet deformation due to compression may be negligible.

In Fig. 8 the comparison of respectively measured p_2 is shown together with the correlation of the PAS as derived from the dynamic pressure proportion of the pitot-tube

AMTD
8, 13423–13469, 2015

measurements. The correlations of the individually measured p_2 between NIXE-CAPS and CCP (Fig. 8, upper-left panel) and between PIP and CCP (Fig. 8, upper-right panel) agree almost in line with the displayed 1 : 1 relationship (dashed red lines). Thus, the p_2 measurement of the instruments does not seem to be significantly affected, neither by the individual probe head design nor by the respective wing position. Note that the calibrated pressure transducers commonly integrated in the individual probes are of the type Honeywell, model 142PC15A with a specified linearity within ±0.4 % of the output signal span for the pressure range between 140 and 1030 hPa. When comparing the PAS obtained from the individual instruments a feature sticks out that seems to solely result from influences on the dynamic pressure from measurements with the pitot-tube.

The dynamic pressure for calculating the air speed results from the total pressure, impacting on the pitot's forward facing congestion tube, subtracted by the static pressure that is detected at the pitot-tube's flanks. Hence, the PAS comparison between NIXE-CAPS and CCP (Fig. 8, lower-left panel) exhibits a systematic discrepancy of about 5–10 $\mathrm{m\,s^{-1}}$ by which the resulting PAS of the CCP exceeds the NIXE-CAPS measurements over the entire velocity range. This may result from different calibrations of the respective pitot-tube or it could be an effect of the instrument's wing position. It is also likely that the systematically stronger deceleration of air flow upstream of NIXE-CAPS is caused by its winglet (cf. Fig. 5) which may increase the probe's cross-sectional-area compared to that of the CCP. Apparently the PAS measured by the PIP increasingly deviates from the CCP-PAS as a function of flight speed. Therefore, the deviation is not of a constant character, but rather increases with increasing flight speed. This shows that the extraordinary behaviour of $\frac{\mathrm{PAS}}{\mathrm{TAS}}$ over the range of flight velocity (cf. Fig. 6, right panel) is only connected to the dynamic pressure proportion obtained from the PIP's pitot-tube measurements. Unless the PIP could be deployed at another HALO underwing position, at least for one flight for investigating this issue more closely, it appear conceivable that the effect originates from an external interference due the PIP's proximity either to the wing root or to the fuselage of HALO. For comparably much smaller flight velocities ($< 100\,\mathrm{m\,s^{-1}}$) previous studies demonstrated that the air flow field changes along the

AMTD
8, 13423–13469, 2015

wing span with different impact on instruments positioned outboard or inboard at an aircraft's wing (Drummond and MacPherson, 1985; MacPherson and Baumgardner, 1988).

For providing a parameterisation of ξ-values as a function of TAS the data set needs to be reassessed by accounting for the limited periods of tamped or malfunctioning pitot-tubes. For the following, those periods that were identified to be affected by an inoperative pitot-tube have been removed from the data set. In Fig. 9 the derived ξ-factor is depicted as a function of TAS. The parameterisation results from fitting a quadratic regression (Table 1) to the given data set. For each instrument the individually derived parameters of v_2 (PAS), and p_2 (static air pressure at the probe) are used, such that the ξ-factors are also individually determined for each instrument. The regression fits in Fig. 9 are provided together with the 95 %-confidence band (blue lines) and the 95 %-prediction band (red lines). Note, that the 95 %-confidence band is very narrow, even covering the black regression fit because the data set used for these regressions is large and the data variability is small. The fit parameters are summarised in Table 1 and the regressions generally reveal values of r^2 greater than 0.95, which confirms the solidity of the functional relationship between ξ and TAS.

3.3 The consistency of ξ for HALO instruments

Further insight into the properties of ξ is provided by Fig. 10 that illustrates the correlation of individually derived ξ-values for each instrument. The ξ-data are color-coded according to TAS and the linear correlation between the instrument-specific ξ-data and TAS are derived. The graphs also contain the very narrow 95 %-confidence band (blue lines) and the 95 %-prediction band (red lines). The parameters for the linear correlations shown in Fig. 10 are also summarised in Table 1. Generally the ξ-values exhibit a strong correlation with a correlation coefficient r^2 larger than 0.97, which indicates ξ to be widely independent of the instrument characteristics, such as wing position or design, in contrast to $\frac{\mathrm{PAS}}{\mathrm{TAS}}$. Nevertheless, in detail the individual ξ-values obviously differ from each other, which is presumably connected to the differently shaped probe

AMTD
8, 13423–13469, 2015

heads or the instrument's distance to the aircraft fuselage. Starting with neighboured instruments, i.e. comparing CCP with NIXE-CAPS (Fig. 10, left panel) and PIP with NIXE-CAPS (Fig. 10, centred panel), an increasing deviation from the 1 : 1 relationship (dashed black lines) appears. This deviation increases with the distance between the instruments, i.e. between the PIP and the CCP (Fig. 10, right panel). It remains speculative to connect the deviation of the individual ξ-values to a relative distance from the aircraft fuselage, i.e. insinuating an impact on the measurements due to the flow field along the fuselage, or to ascribe the deviation to the characteristic instrument design.

3.4 Effectiveness of ξ-corrections on atmospheric particle measurements

In the following the derived ξ-values are applied to data of atmospheric cloud measurements that were performed during the HALO mission ACRIDICON-CHUVA. The studies of various types of tropical convective cells aimed at, amongst other characteristics, the microphysical properties of cloud elements under variable conditions. Large contiguous cloud fields with liquid or mixed-phase cloud particles where probed, occasionally over more than 30 min without encountering cloud-free air. Relatively high particle number concentrations were detected. For demonstrating the effectiveness of the ξ–correction a segment was selected from flight "AC13" on 19 September 2014 between 20:00:40 UTC (72 040 s of day) and 20:32:00 UTC (73 920 s of day). During this flight period, at almost constant level flight at about 13 km altitude (cf. Table 2), spheroid particles were mostly present and detected as such. Figure 11 shows a time series (left panel) of the total number concentration (as 10 s running averages) derived from measurements of both the CCP (CDP and CIPgs) and the PIP. Additionally, a particle size distribution covering the full diameter detection range of CCP and PIP is provided (Fig. 11, right panel) averaged over the complete level flight period to reduce the counting error level to a minimum over the full diameter range covered. In both graphics, the time series and according particle size distribution are shown in three ways:

AMTD
8, 13423–13469, 2015

1. measured particle number concentration N_{meas} (black),
2. the data corrected by values of ξ determined for each second of measurement (green) and
3. the data set after correction with1 Hz-resolved factors of $\frac{PAS}{TAS}$ (red).

The averaged TAS ($\sim 220\,m\,s^{-1}$, cf. Table 2) over the depicted time period suggests a ξ-value that causes an effective correction of N_{meas} of about 10 %, read off Fig. 9. The averaged values of calculated ξ for the CCP and PIP are indeed close to 0.9 (cf. Table 2). However, a correction with $\frac{PAS}{TAS}$ would cause a downscaling of N_{meas} by up to 27 % (for the CCP-detected particle size range, cf. Table 2). In essence, the effective correction of N_{meas} by ξ to obtain N_{amb} may not be excessive but with knowing the variables to determine ξ a systematic bias in measured particle number concentrations is easily eliminated. Finally, if, for example, the Liquid Water Content (LWC) or Ice Water Content (IWC) is extracted from OAP data, a compression correction of N_{meas} over the range of particle sizes may be valuable.

3.5 Correction factor ξ for other fast flying aircraft

Provided that ξ was sufficiently proven to hold for large ranges of atmospheric conditions and aircraft speeds, the question arises whether the properties of ξ can also hold for other fast flying aircraft.

In Fig. 12a the determined ξ-values for each time of CCP measurement on board the Learjet-35A are displayed from a single flight (over 3.3 flight hours) on 5 September 2013 during the AIRTOSS-ICE (AIRcraft TOwed Sensor Shuttle) mission aiming at ice clouds (cirrus) over Northern Germany (Finger et al., 2015). The ξ-values for one flight, when CCP was deployed on an underwing position of the Learjet-35A, are parameterised by means of a quadratic regression and according coefficients are summarised in Table 3. The derived ξ-values (green dots) as a function of TAS follow in general the expected course and the data set is similarly compact over the TAS-range

AMTD
8, 13423–13469, 2015

as previously shown for the HALO cases. However, the comparison of the ξ-fit from the Learjet-35A measurements with the parameterised ξ from HALO-flights (dark cyan line) reveals that ξ for the Learjet-35A configuration generally causes a smaller correction of N_{meas} to reach N_{amb}. As the instruments deployed on board of HALO and the Learjet-35A are identical the systematic difference in ξ indicates that the compression may depend on the instrument-platform-configuration. As ξ is principally a measure for the compression strength, it seems that upstream of the CCP on the Learjet-35A, for some reason, the air compression is weaker than on HALO. Factually, the instrument configuration by using the AIRTOSS, that is released from the Learjet-35A on a steel cable during flight (Frey et al., 2009), displaces the CCP measurements to a certain distance (up to 4000 m) away from any potential source of disturbance or interference provided by the aircraft. The data sets of two flights of the AIRTOSS-ICE campaign were selected which provide all variables required to determine ξ. Measurements during curved manoeuvres were discarded from further analysis as the adaptation of the AIRTOSS's flight attitude to rough changes in flight direction is delayed. Moreover, the CCP pressure data were adjusted to account for the difference of static air pressure accompanied with the lower flight altitude of AIRTOSS with respect to the Learjet-35A. For the levitating CCP the calculated ξ-values are displayed in Fig. 12b (purple dots) exhibiting a strong scatter. However, hereby a dispersion of ξ about a mean appears to be indicated that is close to the ξ-parameterisation fit of measurements with CCP when attached under the Learjet's wing. Thus, a significant influence of the aircraft's wings or the fuselage of the Learjet-35A on the underwing-mounted CCP is not definitely verifiable. Concerning the difference of ξ resulting from measurements either on the Learjet-35A or the G-550 HALO we can only surmise that a specific flow field is induced due to the specific HALO configuration, by the aircraft fuselage and/or the wings' leading edge and/or the pairwise configuration of the underwing instruments. Nevertheless, by applying ξ the individual and systematic influences on the actual thermodynamic conditions under which the measurements occur are, to a large extent, accounted for –

AMTD
8, 13423–13469, 2015

independent on the probably various and likely interfering sources of disturbances on the measurement conditions.

4 Summary and conclusions

Based on thermodynamic considerations, the correction factor ξ is introduced for inverting particle concentrations from measurement conditions to ambient conditions. An equation is provided for deriving ξ that depends on the variables of static pressure and temperature in the ambient (undisturbed) state as well as the aircraft True Air Speed (TAS). Additionally the static pressure measurement and the actually measured air speed (PAS) at the individual probe are needed. Provided that an underwing probe is equipped with a pitot-tube for continuous measurement of air speed and static pressure in the vicinity of the probe, the instrument specific ξ can be derived for each second of measurement during a flight.

Strong indication for the trustworthiness of PAS, individually measured by probes that are equipped with a pitot-tube, is given by the imaging technique of OAP instruments. As the detector scanning of OAPs is triggered by the measured airflow velocity, a significant deviation or falsification of the pitot-measured PAS would result in visibly distorted images. Consequently, the individually measured PAS most likely reflects the air speed at the respective instrument as well as the speed of the particles while penetrating the instrument's detection region. The systematic difference between the air speeds TAS and PAS, particularly at increased flight velocities (i.e. $> 170\,\mathrm{m\,s^{-1}}$), is mainly induced by the compression of air due to an effective surface perpendicular to the air flow provided by the body of the underwing probes. As a result we conclude that there are at present three different approaches to treat particle microphysical data obtained from underwing probes:

a. Without knowledge of the air speed and static pressure at the point of measurement it is common practice to presume that particles penetrate the probe's sample area A_s with speeds equal to the aircraft TAS. Taking this route, the compression

AMTD
8, 13423–13469, 2015

of air due to the moving instrument body and the compression-induced motion of particles out of their ambient (undisturbed) state is ignored. As a consequence of the compression upstream of a probe, the air speed (PAS) and the particle speed at the point of measurement must be systematically lower compared to TAS. Determining particle number concentrations by using the TAS without adjustments regarding the compression leads to an underrepresentation of particle concentrations that is not negligible.

b. The measured particle number concentration N_{meas} (based on the recorded PAS, cf. Paragraph 2.1 for details) does not represent the ambient number concentration of cloud particles. The compression of air causes a modification of the particle's environment and behaviour at the point of measurement compared to ambient (undisturbed) conditions. Thus, the measured particle number concentrations without any corrections may be representative for the measurement conditions only. However, compared to ambient particle number concentrations, the uncorrected N_{meas} is an overestimate of increasing strength with flight velocity. Note that an uncertainty of N_{meas} remains due to the PAS uncertainty which may not considerably exceed 10 %.

c. Multiplying measured particle number concentrations N_{meas} with the ratio $\frac{PAS}{TAS}$, as practiced, with the attempt to hereby invert the measured concentrations to ambient conditions lacks any physical rationale. The ratio of air speeds does not account for the compression of air upstream of the probe which is the major reason for the deviation of measured air speeds, PAS and TAS. By using the ratio $\frac{PAS}{TAS}$, the increase of pressure and the heating accompanied with the compression of air remains fully ignored. Hence, this simplified correction procedure turns out to cause an unreasonable reduction of particle number concentrations. This procedure was shown to affect the results at surprisingly low aircraft speeds. Contrarily, the impact of this procedure was demonstrated to depend on the instruments' underwing position with respect to the aircraft fuselage.

AMTD
8, 13423–13469, 2015

Therefore, the particle number concentration under measurement conditions N_{meas} (based on the recorded PAS, cf. Paragraph 2.1) needs correction to account for the compression of air and the compression-induced motion of particles out of their ambient (undisturbed) state. The herein introduced correction factor ξ covers the most important impacts accompanied with the compression to invert the measured data to ambient conditions.

If pitot-tube measurements are not available the provided ξ-parameterisation as a function of TAS serves as a guideline for adaptation of the TAS to determine particle number concentrations. The parameterisation also shows that the compression effect is comparatively small for lower flight velocities. For a mean cruising speed, e.g. of the M-55 Geophysica of about 170 $m\,s^{-1}$, the systematic bias of the number concentration obtained from CCP measurements may be at most 6 % in the case that the compression is not otherwise accounted for and if the measured number concentrations are directly determined by using the recorded PAS. Note that this potential bias of CCP measurements on board the M-55 Geophysica is directly taken from the parameterisation of ξ for the CCP on HALO (cf. Fig. 9) and therefore represents the uppermost extreme. For slower aircraft, e.g. the POLAR 5 (a modified and turboprop-engined Douglas DC-3) with cruising speed of about 70 $m\,s^{-1}$ (Klingebiel et al., 2015) the potential bias of uncorrected CCP-measured particle number concentrations is at worst 2 % and therefore lies well within the measurement uncertainty. Calculated ξ from CCP measurements on board the Learjet-35A, reaching flight velocities comparable to those of the G-550 HALO, reveals that the compression is generally less expressed in the Learjet-35A configuration compared to that of the G-550 HALO. An increased compression effect on the G-550 HALO is not unambiguously connectable to a specific source. It can only be surmised that on the G-550 HALO a strengthened disturbance on the thermodynamic conditions of underwing probe measurements is accompanied with interferences of the aircraft fuselage and/or the wings' leading edge and/or the pairwise configuration of the underwing instruments.

AMTD
8, 13423–13469, 2015

This study provides a starting point for further intensive instrumental comparisons and investigation by means of combined measurement results of cloud- and aerosol probes from the accomplished HALO field missions ML-CIRRUS and ACRIDICON-CHUVA. However, to make the measurements comparable, a common standard of treating the data and of considering systematic influences on the measurement is essential. This standard needs to be designed and agreed upon before comparing or interpreting the data. The introduced ξ-correction may serve as one contributing factor accounting for the most significant impacts due to compression resulting from the moving instrument body in the medium air on fast flying aircraft. Further flow disturbances due to aircraft components (e.g. the impact of turbulences along the wings, or the flow impacts induced by the fuselage, etc.) are potentially not covered by the ξ-correction but may be subject of detailed Computational Fluid Dynamics (CFD) simulations.

Acknowledgements. The authors thank the coordinators of the involved missions. We gratefully acknowledge the technical support provided by C. v. Glahn, K.-D. Wilhelm, W. Schneider and T. Böttger. We thank for the fruitful discussions with, M. Schnaiter, E. Järvinen, P. Reutter, M. Szakáll, M. Hermann, K. Kandler, and M. Baumgartner essentially contributing this examination as also for the suggestions of the ML-CIRRUS team (ML-CIRRUS workshop, 25–26 November 2015). Furthermore the help and advices of R. E. Jubb are highly appreciated as well as the very valuable and constructive suggestions of D. Baumgardner. This work is based on data acquired during the DFG-supported (SPP1294) HALO missions ML-CIRRUS and ACRIDICON-CHUVA, and this study was prepared with support by the German "Bundesministerium für Bildung und Forschung" (BMBF) within the joint ROMIC-project SPITFIRE (01LG1205A). The AIRTOSS-ICE campaign was supported by DFG through the projects BO1829/7-1 and SP1163/3-1. Our research received funding from the European Research Council under the European Union's Seventh Framework Program (FP/2007-2013)/ERC Grant Agreement No. 321040 (EXCATRO). Financial support from the Max-Planck-Institute for Chemistry and the Helmholtz-society is gratefully acknowledged. We particularly thank all aircraft crew members and operators of the research aircraft HALO and the GFD Learjet-35A for their engagement.

AMTD
8, 13423–13469, 2015

References

Baumgardner, D., Strapp, W., and Dye, J. E.: Evaluation of the forward scattering spectrometer probe. Part II: Corrections for coincidence and dead-time losses, J. Atmos. Ocean. Tech., 2, 626–632, doi:10.1175/1520-0426(1985)002<0626:eotfss>2.0.co;2, 1985.

Baumgardner, D., Jonsson, H., Dawson, W., O'Connor, D., and Newton, R.: The cloud, aerosol and precipitation spectrometer: a new instrument for cloud investigations, Atmos. Res., 59–60, 251–264, doi:10.1016/S0169-8095(01)00119-3, 2001.

Baumgardner, D., Brenguier, J. L., Bucholtz, A., Coe, H., DeMott, P., Garrett, T. J., Gayet, J. F., Hermann, M., Heymsfield, A., Korolev, A., Krämer, M., Petzold, A., Strapp, W., Pilewskie, P., Taylor, J., Twohy, C., Wendisch, M., Bachalo, W., and Chuang, P.: Airborne instruments to measure atmospheric aerosol particles, clouds and radiation: a cook's tour of mature and emerging technology, Atmos. Res., 102, 10–29, doi:10.1016/j.atmosres.2011.06.021, 2011.

Baumgardner, D., Newton, R., Krämer, M., Meyer, J., Beyer, A., Wendisch, M., and Vochezer, P.: The Cloud Particle Spectrometer with Polarization Detection (CPSPD): a next generation open-path cloud probe for distinguishing liquid cloud droplets from ice crystals, Atmos. Res., 142, 2–14, doi:10.1016/j.atmosres.2013.12.010, 2014.

Dixon, J. C.: Appendix B: properties of air, in: The Shock Absorber Handbook, John Wiley & Sons LTD, Chichester, UK, 375–378, 2007.

Drummond, A. M. and MacPherson, J. I.: Aircraft flow effects on cloud drop images and concentrations measured by the NAE twin otter, J. Atmos. Ocean. Tech., 2, 633–643, doi:10.1175/1520-0426(1985)002<0633:afeocd>2.0.co;2, 1985.

Dye, J. E. and Baumgardner, D.: Evaluation of the forward scattering spectrometer probe. Part I: Electronic and optical studies, J. Atmos. Ocean. Tech., 1, 329–344, doi:10.1175/1520-0426(1984)001<0329:eotfss>2.0.co;2, 1984.

Finger, F., Werner, F., Klingebiel, M., Ehrlich, A., Jäkel, E., Voigt, M., Borrmann, S., Spichtinger, P., and Wendisch, M.: Spectral optical layer properties of cirrus from collocated airborne measurements – a feasibility study, Atmos. Chem. Phys. Discuss., 15, 19045–19077, doi:10.5194/acpd-15-19045-2015, 2015.

Frey, W., Eichler, H., de Reus, M., Maser, R., Wendisch, M., and Borrmann, S.: A new airborne tandem platform for collocated measurements of microphysical cloud and radiation properties, Atmos. Meas. Tech., 2, 147–158, doi:10.5194/amt-2-147-2009, 2009.

AMTD
8, 13423–13469, 2015

Frey, W., Borrmann, S., Kunkel, D., Weigel, R., de Reus, M., Schlager, H., Roiger, A., Voigt, C., Hoor, P., Curtius, J., Krämer, M., Schiller, C., Volk, C. M., Homan, C. D., Fierli, F., Di Donfrancesco, G., Ulanovsky, A., Ravegnani, F., Sitnikov, N. M., Viciani, S., D'Amato, F., Shur, G. N., Belyaev, G. V., Law, K. S., and Cairo, F.: In situ measurements of tropical cloud properties in the West African Monsoon: upper tropospheric ice clouds, Mesoscale Convective System outflow, and subvisual cirrus, Atmos. Chem. Phys., 11, 5569–5590, doi:10.5194/acp-11-5569-2011, 2011.

Hinds, W. C.: Aerosol Technology: Properties, Behavior, and Measurement of Airborne Particles (2nd edition), John Wiley & Sons LTD, Chichester, UK, 1999.

Kärcher, B. and Lohmann, U.: A parameterization of cirrus cloud formation: Homogeneous freezing of supercooled aerosols, J. Geophys. Res.-Atmos., 107, 4010, doi:10.1029/2001jd000470, 2002.

Klingebiel, M., de Lozar, A., Molleker, S., Weigel, R., Roth, A., Schmidt, L., Meyer, J., Ehrlich, A., Neuber, R., Wendisch, M., and Borrmann, S.: Arctic low-level boundary layer clouds: in situ measurements and simulations of mono- and bimodal supercooled droplet size distributions at the top layer of liquid phase clouds, Atmos. Chem. Phys., 15, 617–631, doi:10.5194/acp-15-617-2015, 2015.

Knollenberg, R. G.: The optical array: an alternative to scattering or extinction for airborne particle size determination, J. Appl. Meteorol., 9, 86–103, doi:10.1175/1520-0450(1970)009<0086:toaaat>2.0.co;2, 1970.

Korolev, A.: Reconstruction of the sizes of spherical particles from their shadow images. Part I: Theoretical considerations, J. Atmos. Ocean. Tech., 24, 376–389, doi:10.1175/jtech1980.1, 2007.

Korolev, A., Makarov, Y. E., and Novikov, V.: On the calibration of photoelectric cloud droplet spectrometer FSSP-100, TCAO, 158, 43–49, 1985.

Korolev, A. V., Kuznetsov, S. V., Makarov, Y. E., and Novikov, V. S.: Evaluation of measurements of particle size and sample area from optical array probes, J. Atmos. Ocean. Tech., 8, 514–522, doi:10.1175/1520-0426(1991)008<0514:eomops>2.0.co;2, 1991.

Korolev, A. V., Strapp, J. W., and Isaac, G. A.: Evaluation of the accuracy of PMS optical array probes, J. Atmos. Ocean. Tech., 15, 708–720, doi:10.1175/1520-0426(1998)015<0708:eotaop>2.0.co;2, 1998.

Krämer, M., Schiller, C., Afchine, A., Bauer, R., Gensch, I., Mangold, A., Schlicht, S., Spelten, N., Sitnikov, N., Borrmann, S., de Reus, M., and Spichtinger, P.: Ice supersaturations

AMTD
8, 13423–13469, 2015

and cirrus cloud crystal numbers, Atmos. Chem. Phys., 9, 3505–3522, doi:10.5194/acp-9-3505-2009, 2009.
Kulkarni, P., Baron, P. A., and Willeke, K.: Aerosol Measurement: Principles, Techniques, and Applications, John Wiley & Sons LTD, Chichester, UK 2011.
Lance, S., Brock, C. A., Rogers, D., and Gordon, J. A.: Water droplet calibration of the Cloud Droplet Probe (CDP) and in-flight performance in liquid, ice and mixed-phase clouds during ARCPAC, Atmos. Meas. Tech., 3, 1683–1706, doi:10.5194/amt-3-1683-2010, 2010.
Laursen, K. K., Jorgensen, D. P., Brasseur, G. P., Ustin, S. L., and Huning, J. R.: HIAPER: the next generation NSF/NCAR research aircraft, B. Am. Meteorol. Soc., 87, 896–909, doi:10.1175/bams-87-7-896, 2006.
Lawson, R. P., O'Connor, D., Zmarzly, P., Weaver, K., Baker, B., Mo, Q., and Jonsson, H.: The 2D-S (Stereo) probe: design and preliminary tests of a new airborne, high-speed, high-resolution particle imaging probe, J. Atmos. Ocean. Tech., 23, 1462–1477, doi:10.1175/jtech1927.1, 2006.
MacPherson, J. I. and Baumgardner, D.: Airflow about king air wingtip-mounted cloud particle measurement probes, J. Atmos. Ocean. Tech., 5, 259–273, doi:10.1175/1520-0426(1988)005<0259:aakawm>2.0.co;2, 1988.
Meyer, J.: Ice Crystal Measurements with the New Particle Spectrometer NIXE-CAPS, Schriften des Forschungszentrums Jülich: Energy & Environment 160, Jülich, Germany, 2012.
Molleker, S., Borrmann, S., Schlager, H., Luo, B., Frey, W., Klingebiel, M., Weigel, R., Ebert, M., Mitev, V., Matthey, R., Woiwode, W., Oelhaf, H., Dörnbrack, A., Stratmann, G., Grooß, J.-U., Günther, G., Vogel, B., Müller, R., Krämer, M., Meyer, J., and Cairo, F.: Microphysical properties of synoptic-scale polar stratospheric clouds: in situ measurements of unexpectedly large HNO_3-containing particles in the Arctic vortex, Atmos. Chem. Phys., 14, 10785–10801, doi:10.5194/acp-14-10785-2014, 2014.
Norment, H. and Quealy, A.: Three-dimensional trajectory analyses of two drop sizing instruments: PMS OAP and PMS FSSP, AIAA 25th Aerospace Sciences Meeting, 12–15 January 1987, Reno, Nevada, USA, doi:10.2514/6.1987-180, 1988.
Pruppacher, H. R. and Klett, J. D.: Microphysics of Clouds and Precipitation, Springer, Heidelberg, Germany, 2012.
Spichtinger, P. and Gierens, K. M.: Modelling of cirrus clouds – Part 1a: Model description and validation, Atmos. Chem. Phys., 9, 685–706, doi:10.5194/acp-9-685-2009, 2009.

AMTD
8, 13423–13469, 2015

Voigt, C., Schumann, U., Minikin, A., and Team, A.: ML-CIRRUS – the airborne experiment on natural cirrus and contrail-cirrus with the new 1 High Altitude LOng range research aircraft HALO, B. Am. Meteorol. Soc., BAMS-D-15–00213, 2015.

Wendisch, M. and Brenguier, J.-L.: Airborne measurements for Environmental Research: Methods and Instruments, John Wiley & Sons LTD, Chichester, UK, 2013.

Wendisch, M., Pöschl, U., Andreae, M. O., Machado, L. A. T., Albrecht, R., Schlager, H., Rosenfeld, D., Martin, S. T., Abdelmonem, A., Afchine, A., Araùjo, A., Artaxo, P., Aufmhoff, H., Barbosa, H. M. J., Borrmann, S., Braga, R., Buchholz, B., Cecchini, M. A., Costa, A., Curtius, J., Dollner, M., Dorf, M., Dreiling, V., Ebert, V., Ehrlich, A., Ewald, F., Fisch, G., Fix, A., Frank, F., Fütterer, D., Heckl, C., Heidelberg, F., Hüneke, T., Jäkel, E., Järvinen, E., Jurkat, T., Kanter, S., Kästner, U., Kenntner, M., Kesselmeier, J., Klimach, T., Knecht, M., Kohl, R., Kölling, T., Krämer, M., Krüger, M., Krisna, T. C., Lavric, J. V., Longo, K., Mahnke, C., Manzi, A. O., Mayer, B., Mertes, S., Minikin, A., Molleker, S., Münch, S., Nillius, B., Pfeilsticker, K., Pöhlker, C., Roiger, A., Rose, D., Rosenow, D., Sauer, D., Schnaiter, M., Schneider, J., Schulz, C., de Souza, R. A. F., Spanu, A., Stock, P., Vila, D., Voigt, C., Walser, A., Walter, D., Weigel, R., Weinzierl, B., Werner, F., Yamasoe, M. A., Ziereis, H., Zinner, T., and Zöger, M.: Introduction of the ACRIDICON–CHUVA campaign studying deep convective clouds and precipitation over Amazonia using the new German HALO research aircraft, BAMS-D-14-00255, B. Am. Meteorol. Soc., submitted, 2015.

Willeke, K. and Baron, P. A.: Aerosol measurement, Principles, Techniques and Applications, Van, John Wiley & Sons LTD, Chichester, UK, 1993.

AMTD
8, 13423–13469, 2015

Table 1. Coefficients of the statistical analyses of derived ξ-values: (1) quadratic regression with parameters and standard deviations (σ). (2) linear correlation of the instrument specific ξ-values. Both, the ξ-parameterisations and correlations from HALO measurements are based on > 130 000 single 1 Hz-data points (> 36 flight hours).

Regression for parameterisation of ξ as a function of HALO-TAS: $f = y_0 + a \cdot x + b \cdot x^2$			
	CCP	NIXE-CAPS	PIP
$y_0 \pm \sigma$	$0.99 \pm 2.04 \times 10^{-4}$	$0.99 \pm 2.36 \times 10^{-4}$	$0.98 \pm 4.04 \times 10^{-4}$
$a \pm \sigma$	$3.18 \times 10^{-4} \pm 2.34 \times 10^{-6}$	$2.55 \times 10^{-4} \pm 2.71 \times 10^{-6}$	$4.27 \times 10^{-4} \pm 4.68 \times 10^{-6}$
$b \pm \sigma$	$-3.40 \times 10^{-6} \pm 6.48 \times 10^{-9}$	$-3.30 \times 10^{-6} \pm 7.54 \times 10^{-9}$	$-4.04 \times 10^{-6} \pm 1.31 \times 10^{-8}$
r^2	0.99	0.98	0.96
linear regression of instrument specific ξ inter-correlation: $f = y_0 + a \cdot x$			
	CCP vs. NIXE-CAPS	PIP vs. NIXE-CAPS	PIP vs. CCP
$y_0 \pm \sigma$	$-0.04 \pm 2.26 \times 10^{-4}$	$0.11 \pm 3.54 \times 10^{-4}$	$0.15 \pm 3.38 \times 10^{-4}$
$a \pm \sigma$	$1.03 \pm 2.49 \times 10^{-4}$	$0.88 \pm 3.97 \times 10^{-4}$	$0.85 \pm 3.78 \times 10^{-4}$
r^2	0.99	0.98	0.98

AMTD
8, 13423–13469, 2015

Table 2. Altitude and flight velocity for the ACRIDICON-CHUVA mission flight "AC13" on 19 September 2014 over the time period between 20:00:40 UTC (72 040 s of day) and 20:32:00 UTC (73 920 s of day) and derived corrections of ξ and $\frac{PAS}{TAS}$ for CCP and PIP.

	flight altitude in m a.s.l.	TAS in m s^{-1}	ξ – CCP	ξ – PIP	$\frac{PAS}{TAS}$ – CCP	$\frac{PAS}{TAS}$ – PIP
Average	12 971.6	221.75	0.90	0.87	0.73	0.89
Maximum	12 980.7	226.89	0.91	0.87	0.74	0.90
Minimum	12 962.5	215.12	0.89	0.86	0.72	0.88

AMTD
8, 13423–13469, 2015

Table 3. Coefficients of the statistical analyses of derived ξ-values for CCP measurements on the Learjet-35A: quadratic regression with parameters and standard deviations (σ). The ξ-parameterisation is based on > 12 000 single 1 Hz-data points ($\approx$ 3.3 flight hours).

Regression for parameterisation of ξ as a function of Learjet-TAS: cf. Table 1	
	CCP
$y_0 \pm \sigma$	$0.99 \pm 6.91 \times 10^{-4}$
$a \pm \sigma$	$3.74 \times 10^{-4} \pm 8.35 \times 10^{-6}$
$b \pm \sigma$	$-3.08 \times 10^{-6} \pm 2.48 \times 10^{-8}$
r^2	0.97

AMTD
8, 13423–13469, 2015

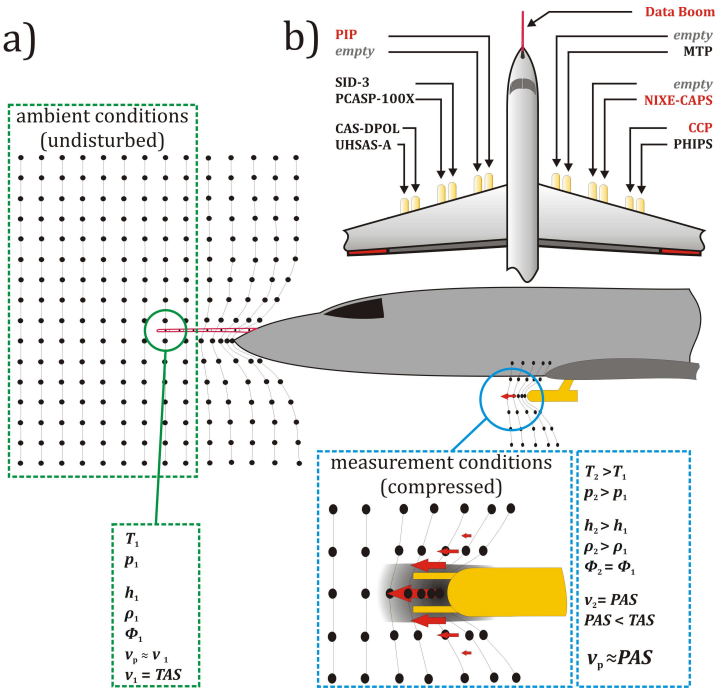

Figure 1. Illustration of the aircraft geometry, different types of probes and their underwing position, and air compression effects. **(a)** The moving aircraft induces an increase of particle concentration in particular upstream of the underwing probes (grey-shaded area). Parameters used for deriving a thermodynamic correction are listed for ambient (undisturbed) conditions (green box) and for measurement conditions (blue box). Note that specified velocities refer to the moving aircraft or instrument relative to the air or the particles. **(b)** The top-view diagram of the aircraft indicates the probe's mounting position during the ML-CIRRUS and the ACRIDICON-CHUVA field missions. Data originating from the probes indicated in red are used for this study. (Instrument name acronyms are specified in the text).

AMTD
8, 13423–13469, 2015

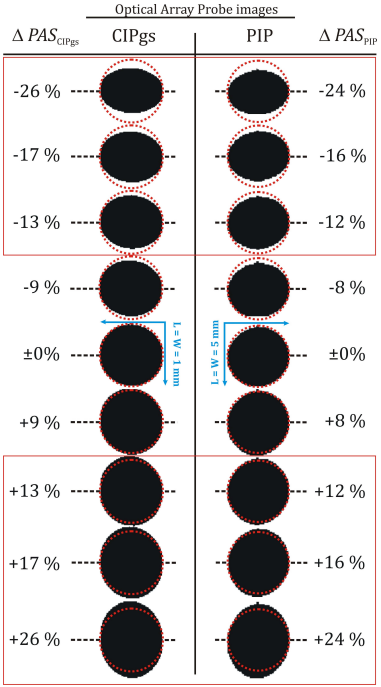

Figure 2. Shadow cast images of non-transparent circular spots on a spinning disk (for calibration purposes) passing the probes' sample area A_s with constant velocity (~ 23–25 m s^{-1}). For this illustration, in the data acquisition program, the air speed (PAS) is manually varied stepwise with the finest available resolution for triggering the timing of imaging. Manually shifting the PAS causes a positive or a negative deviation (ΔPAS) of the air speed relative to the constant disk rotation speed v_{rot}. Deformed images relative to the dashed red circles of identical diameter (according to ΔPAS = ±0 % if v_{rot} = PAS, marked in blue) indicate image distortion that becomes significant for ΔPAS exceeding 10 % (red boxes). PIP images are slightly shifted as v_{rot} of two radially opposed points on the edges of a 5 mm-sized disk spot increases with distance from the disk's centre.

AMTD
8, 13423–13469, 2015

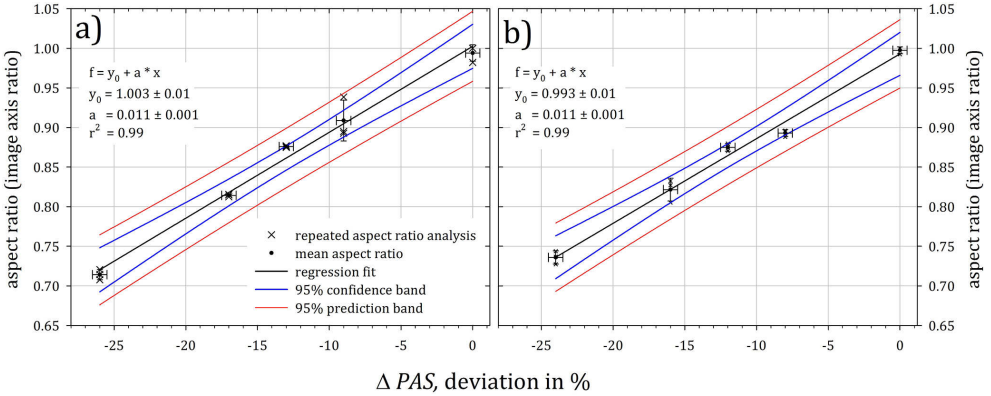

Figure 3. Aspect ratios of taken images as a function of the deviation of the Probe Air Speed (PAS) from the penetration speed of a circular object through the instrument's detection region. The image aspect ratio provides a measure of the distortion strength when the PAS setting is manually shifted in the data acquisition software compared to the constant penetration speed of a circular object on the spinning disc used for calibrations of an Optical Array Probe (OAP). **(a)** for the Cloud Combination Probe's CIP and **(b)** for the Precipitation Imaging Probe (PIP).

AMTD
8, 13423–13469, 2015

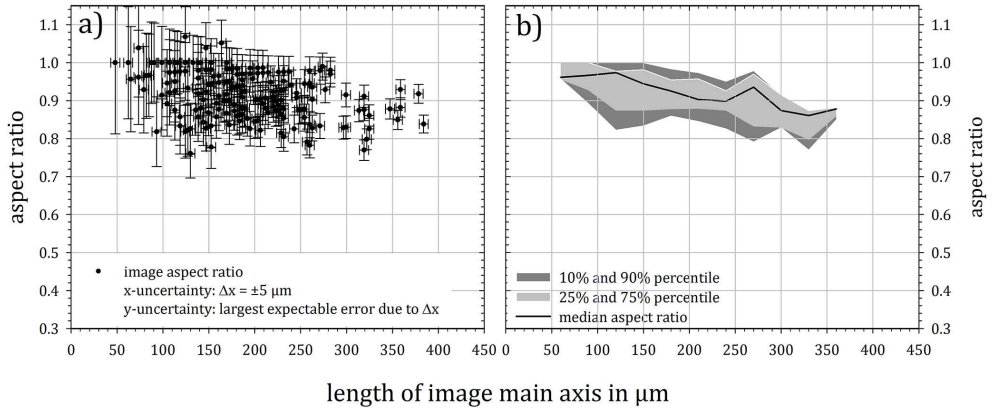

Figure 4. Aspect ratios as a function of the image's main axis dimension as revealed from reanalysis of more than 200 particle images acquired over ~ 6 flight hours during the ACRIDICON-CHUVA mission flight "AC13" on 19 September 2014, over the Amazonian basin, Brazil. Random samples, exclusively of images that indicate to originate from spheroidal objects, were taken well distributed over the data sets recorded during the complete flight. Images of spheroidal objects exhibit particular symmetry and shading intensity compared to other particle species. Flight speeds covered: ~ 41 % of the flight at 200–220 m s^{-1}, ~ 16 % at 140–180 m s^{-1}, ~ 25 % at 120–140 m s^{-1}, ~ 18 % ascents and descents with various flight speeds. **(a)** The measured aspect ratio of the individual images of spheroidal particles, and **(b)** the statistically treated data provided as median of the aspect ratios together with 10 %-, 25 %-, 75 %-, 90 %-percentiles.

AMTD
8, 13423–13469, 2015

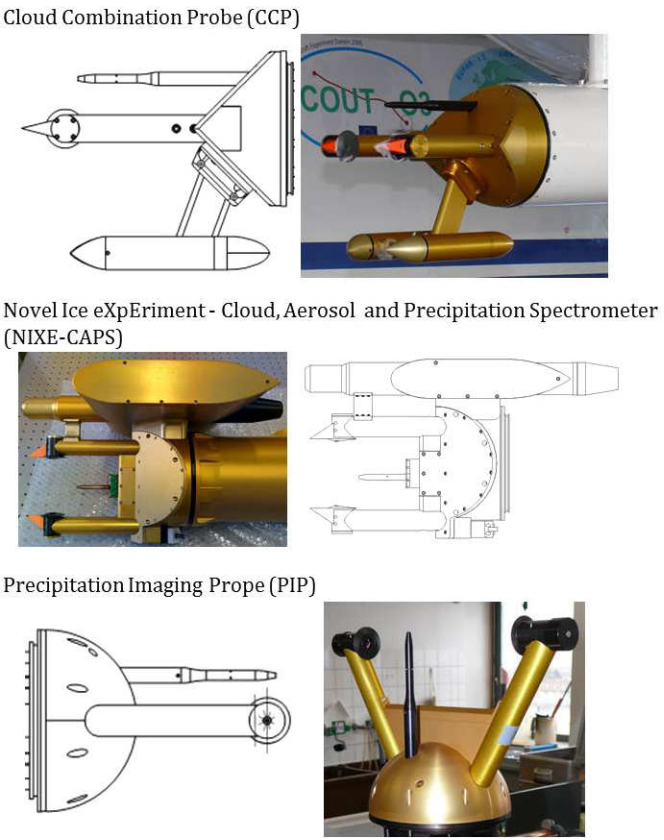

Figure 5. Diagrams and images of the different instrument heads of quasi-streamlined design. Top: Cloud Combination Probe (CCP) with 90°-angled wedge. Middle: combined probe head of 90°-angled wedge and additional winglet of NIXE-CAPS. Bottom: Precipitation Imaging Probe (PIP) with half-sphere probe head.

AMTD
8, 13423–13469, 2015

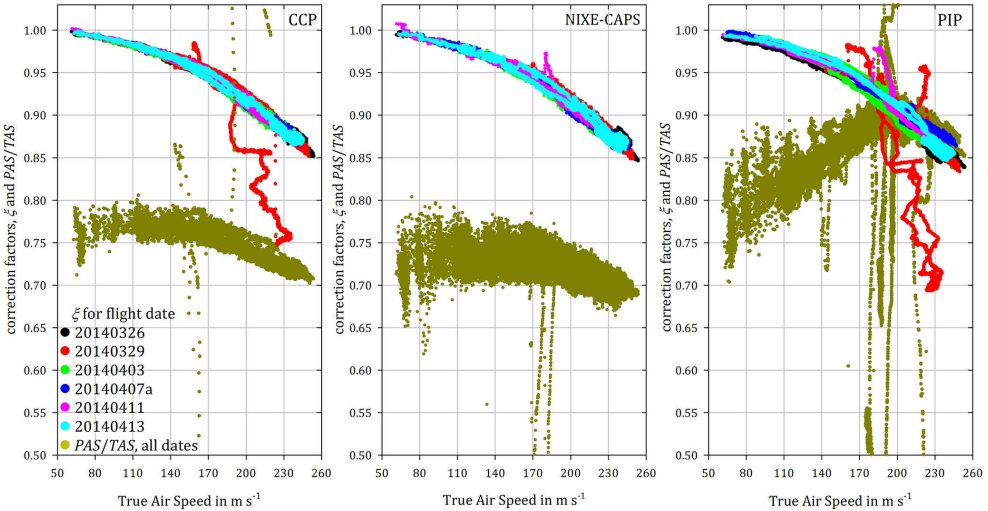

Figure 6. Comparison of two different instrument-specific corrections applied to data acquired on HALO during ML-CIRRUS. The geometric correction $\frac{\mathrm{PAS}}{\mathrm{TAS}}$ causes a general downscaling of measured concentrations of 20 % to up to 35 % for NIXE-CAPS and CCP. Thereby $\frac{\mathrm{PAS}}{\mathrm{TAS}}$ is highly variable, ambiguous and shows significant dependence on the instrument's wing position. At the PIP position (portside, innermost) the behaviour of $\frac{\mathrm{PAS}}{\mathrm{TAS}}$ as a function of TAS is different, presumably due to air flow disturbances by the aircraft's fuselage. Instrument-specific ξ-values exhibits higher compactness over the TAS-range and show reduced dependence on the wing position. The data are from six ML-CIRRUS flights and include outliers due to freezing of the pitot-tubes or due to distortions from isoaxial flow accompanied with manoeuvres such as tight turns.

AMTD
8, 13423–13469, 2015

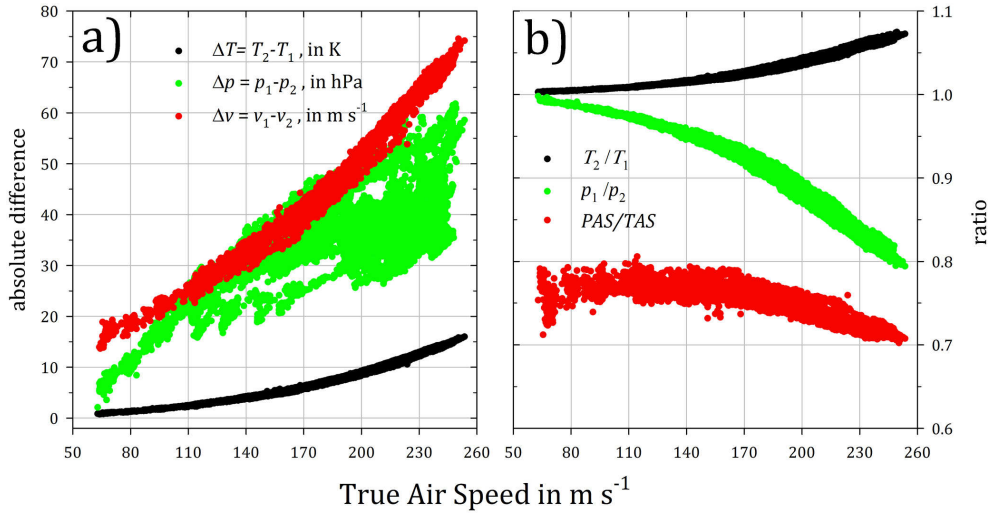

Figure 7. Relevant parameters for determining ξ as a function of TAS for the CCP. **(a)** The absolute difference of measured pressures (p_1, p_2) and velocities (v_1, v_2) and the difference of measured temperature T_1 to calculated T_2. **(b)** The ratio of pressures $\frac{p_1}{p_2}$ and temperatures $\frac{T_2}{T_1}$ as used in Eq. (11) to illustrate respective effectiveness in the ξ-correction.

AMTD
8, 13423–13469, 2015

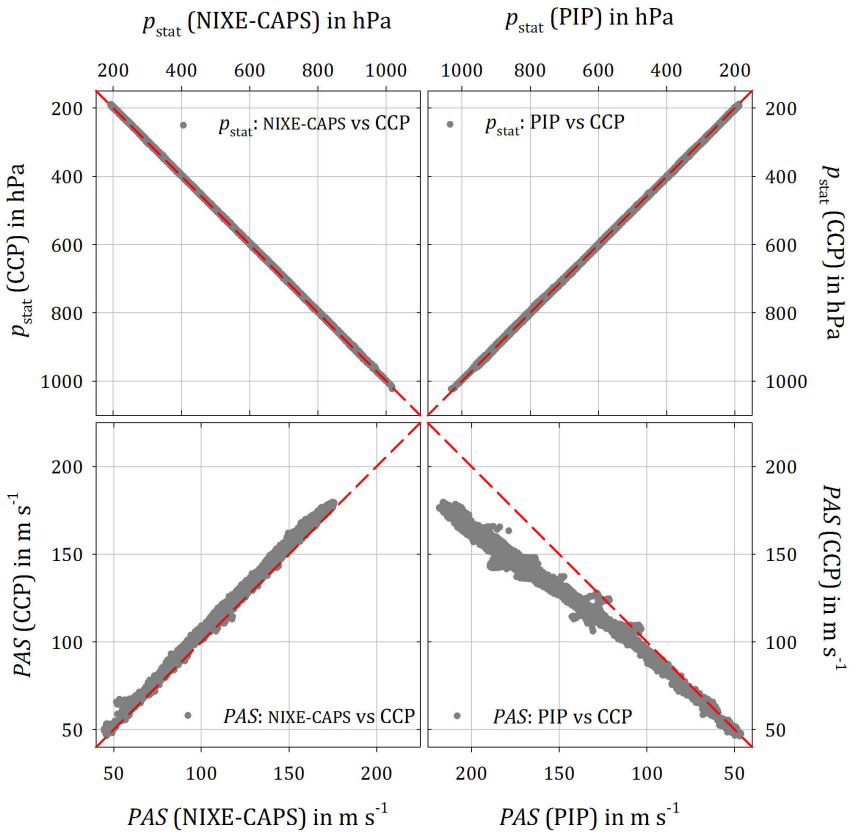

Figure 8. Correlations between individually measured static pressures and PAS for each instrument pair. The p correlations (upper panels) indicate consistency as the data follow the 1 : 1 relationship (dashed red lines). The PAS-correlations (lower panels) reveal systematic deviations from the 1 : 1 relationship, indicative for an unspecified flow disturbance at according instrument position.

AMTD
8, 13423–13469, 2015

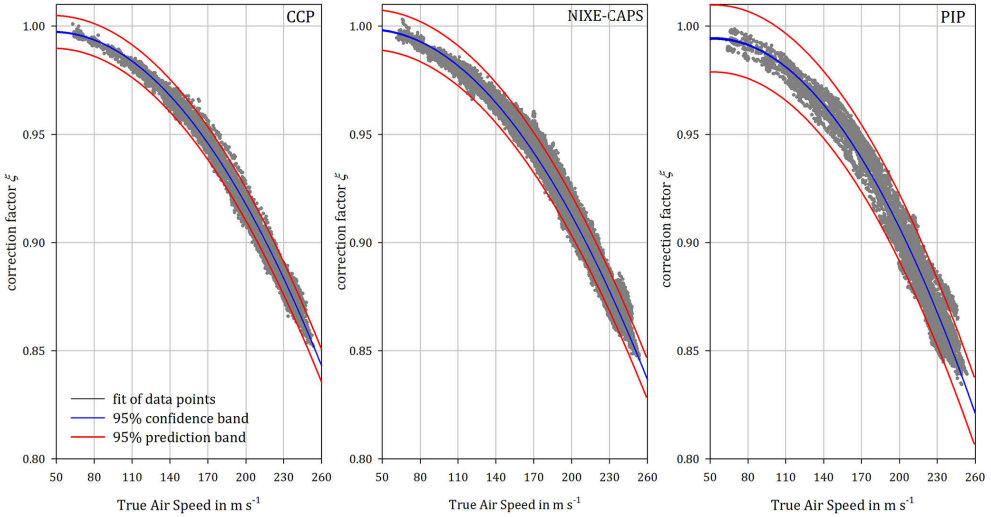

Figure 9. Parameterisation of ξ as a function of TAS for the three different instruments deployed on HALO during the ML-CIRRUS mission. Parameterisation coefficients are provided in Table 1.

AMTD
8, 13423–13469, 2015

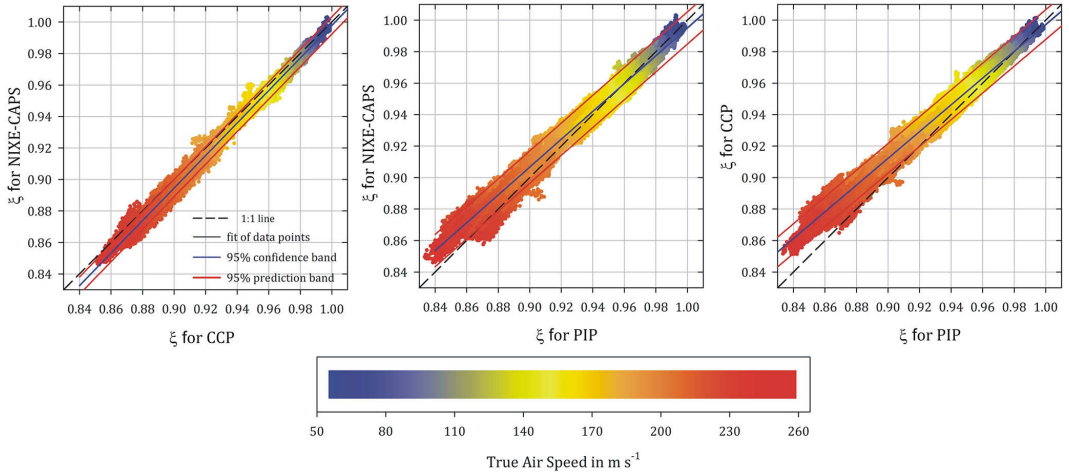

Figure 10. Correlations of instrument-specific ξ.The deviation from the 1 : 1 relationship (dashed black lines) as a function of the aircraft True Air Speed (TAS) is strongest at the PIP position (portside, innermost). Coefficients for the correlations are provided in Table 1.

AMTD
8, 13423–13469, 2015

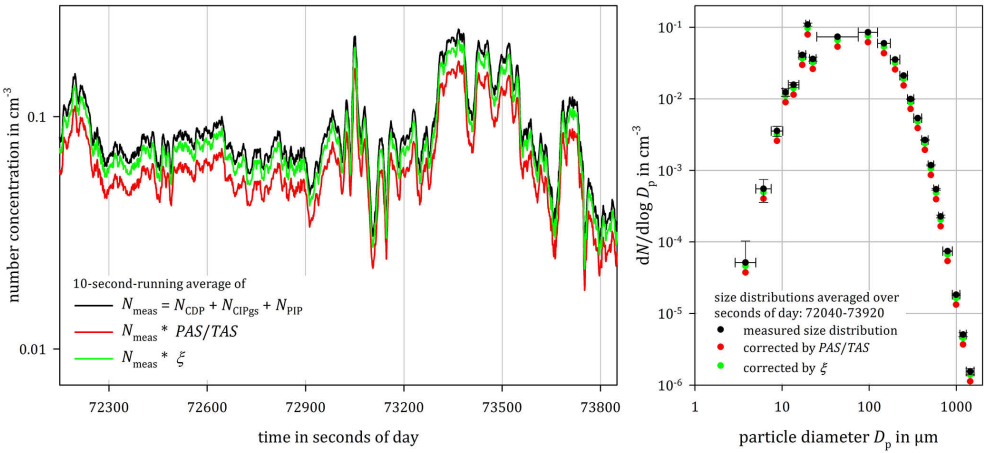

Figure 11. Resulting particle number concentration after application of different correction procedures on data acquired during the ACRIDICON-CHUVA mission flight "AC13" on 19 September 2014 between 20:00:40 UTC (72 040 s of day) and 20:32:00 UTC (73 920 s of day), over the Amazonian basin, Brazil. Left panel: the time series of total particle concentration measured with CCP and PIP. Right panel: the resulting particle size distribution, merged from CCP (CDP and CIPgs) and PIP measurements.

AMTD
8, 13423–13469, 2015

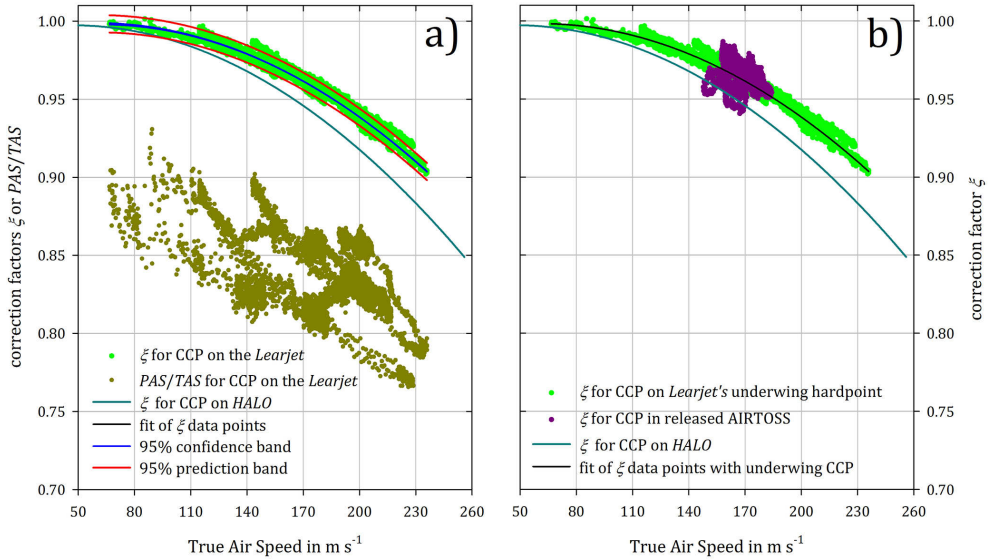

Figure 12. Comparison of corrections for the CCP **(a)** with the CCP attached to a Learjet-35A's underwing hardpoint (flight on 5 September 2013) during the AIRTOSS-ICE mission over Northern Germany. The $\frac{\text{PAS}}{\text{TAS}}$ correction exhibits broad scatter and ambiguities. Instead, the determined ξ-values yield compactness over the complete TAS-range. For comparison the ξ-parameterisation from HALO measurements of the CCP are implied, illustrating the dependence of ξ on the used measurement platform. **(b)** instead of $\frac{\text{PAS}}{\text{TAS}}$ the ξ-values are shown for the CCP when deployed in the AIRcraft TOwed Sensor Shuttle (AIRTOSS) released from the Learjet-35A on a steel cable.

AMTD
8, 13423–13469, 2015